Solid State Ionics 357 (2020) 115468

Contents lists available at ScienceDirect

Solid State Ionics

journal homepage: www.elsevier.com/locate/ssi

Reversible electrochemical potassium deintercalation from > 4 V positive electrode material $K_6(VO)_2(V_2O_3)_2(PO_4)_4(P_2O_7)$

Ivan V. Tereshchenko[a,b], Dmitry A. Aksyonov[a], Andriy Zhugayevych[a], Evgeny V. Antipov[a,b], Artem M. Abakumov[a,*]

[a] Skolkovo Institute of Science and Technology, 3 Nobel St, Moscow 121205, Russian Federation
[b] Lomonosov Moscow State University, 1 bld. 3 Leninskie Gory, Moscow 119991, Russian Federation

ARTICLE INFO

Keywords:
Potassium-ion battery
Cathode
Phosphate
Pyrophosphate
Vanadium
High voltage
Density functional theory
Diffusion

ABSTRACT

Reversible electrochemical deintercalation of potassium from the $K_6(VO)_2(V_2O_3)_2(PO_4)_4(P_2O_7)$ phosphate-pyrophosphate-oxide of potassium and vanadium (IV,V) obtained through a ceramic route has been demonstrated. The material has been tested as a high voltage positive electrode (cathode) for K-ion batteries, demonstrating 53% of the theoretical capacity of 88 mAh/g at the current density C/50 in the 1.8–4.4 V vs K/K^+ potential range. The crystal structures of $K_6(VO)_2(V_2O_3)_2(PO_4)_4(P_2O_7)$ in the pristine, charged and discharged states were refined by Rietveld method from powder X-ray diffraction data using a structure model with stochastic orientation of the pyrophosphate groups (space group *Pnma*, a = 6.9891(1)Å, b = 13.3735(2)Å, c = 14.2495(2)Å in the pristine state). In spite of deintercalation of bulky K^+ cations, the cell volume change upon charge amounts to 0.9% rendering $K_6(VO)_2(V_2O_3)_2(PO_4)_4(P_2O_7)$ a "low strain" cathode. The potassium (de)intercalation occurs equally from two distinct crystallographic sites through a single ~4.2 V sloped plateau featuring solid-solution-like behavior, which was demonstrated by *operando* powder X-ray diffraction. The evaluation of diffusion barriers from the first principles has been conducted by the nudged elastic band method for two ordered arrangements of the pyrophosphate groups derived from the refined disordered structure. The diffusion barriers along crystallographic direction *b* for both investigated ordered variants were found to be below 0.3 eV.

1. Introduction

In spite of rich chemistry of complex compounds of potassium and transition metals, the variety of possible candidates for positive electrode (cathode) materials for K-ion batteries (PIBs) is by far more restricted compared to that for the Li-ion or Na-ion batteries. Among these candidates are the cyanometallate complexes [1–4], oxide- and fluoride-phosphates [5–8] and sulfates [9], layered oxides [10–14] and very few polyanion compounds [15,16]. As the PIBs might provide a viable alternative to LIBs due to lower price and higher abundance of potassium, the search for new structures suitable for reversible potassium intercalation is of great interest. The electrochemical capacity of the K-based cathode materials is generally lower than the capacity of their Li- or Na-based counterparts. Thus it is vitally important for K-ion batteries to maintain practically viable energy density through implementation of the cathode materials with higher working potential [17]. A well-known way to raise the redox potential of the $M^{n+}/M^{(n+1)+}$ (M – transition metal) redox pair is through inductive effect of polyanion groups increasing the ionicity of the M-O bonds because of their higher electronegativity compared to that of oxide anions [18]. The pyrophosphate $P_2O_7^{4-}$ group is considered more electronegative than the phosphate PO_4^{3-} group as it provides more resonant forms for electron delocalization [18]. As an example, the discharge of the $K_3V_2(PO_4)_3$ cathode material occurs through two pseudo-plateaus at ~3.6 and 3.9 V vs K/K^+ [15], whereas the same V^{3+}/V^{4+} redox pair in KVP_2O_7 demonstrates the discharge plateaus at much higher potentials of ~4.0 and 4.4 V [16].

In the present work we have blended the phosphate and pyrophosphate groups in the crystal structure of a complex phosphate-pyrophosphate-oxide of potassium and vanadium (IV,V) $K_6(VO)_2(V_2O_3)_2(PO_4)_4(P_2O_7)$ (Fig. 1) [19] to test this material as a cathode for PIBs with the theoretical capacity of 132 mAh/g (assuming full potassium extraction) or 88 mAh/g (assuming complete V(IV) to V (V) oxidation). We demonstrated the reversible potassium deintercalation through a single ~4.2 V sloped plateau on charge/discharge delivering ~53% of the theoretical capacity. The analyzed structural changes upon electrochemical cycling point to a solid solution (de)intercalation mechanism. These results demonstrate that the design of

* Corresponding author.
E-mail address: a.abakumov@skoltech.ru (A.M. Abakumov).

https://doi.org/10.1016/j.ssi.2020.115468
Received 5 July 2020; Received in revised form 23 September 2020; Accepted 25 September 2020

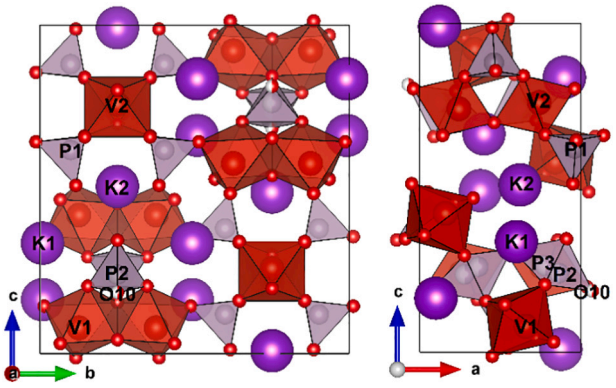

Fig. 1. Two projections of the $K_6(VO)_2(V_2O_3)_2(PO_4)_4(P_2O_7)$ subcell. The V1 position contains V(IV) and V(V) in a 1:1 ratio, which are ordered in the supercell, and V2 contains only V(IV). The P1 position belongs to the PO_4 phosphate group, whereas the P2 and P3 positions belong to the P_2O_7 pyrophosphate groups. Splitting of the P2, P3 and O10 positions indicate positional disorder in the subcell, which is eliminated in the supercell.

multipolyanionic compounds may lead to further expansion of the > 4 V class of cathodes for the K-ion batteries.

2. Experimental

$K_6(VO)_2(V_2O_3)_2(PO_4)_4(P_2O_7)$ has been synthesized via a two-stage ceramic route. On the first stage 0.573 g of V_2O_5 (Sigma Aldrich, 98%) were introduced into aqueous solution containing 2.8125 g of $H_2C_2O_4$ (Sigma Aldrich, 98%), 0.850 g of KH_2PO_4 (Реахим, 99%) and 10 ml of deionized water. After stirring for 30 min in air the greenish-blue colour characteristic of vanadium (IV) was established. Then additionally 5.63 g of D-glucose (Sigma Aldrich, 99.5%) were dissolved, the obtained solution was dried and the residue was calcined in air in a muffle furnace at 350 °C for 5 h. Yellowish-green foam obtained after the calcination was thoroughly grinded in a mortar and pressed into a pellet. The pellet was calcined at 425 °C for 4 h under Ar flow with the residual oxygen content $< 2{\cdot}10^{-4}$ vol%.

Phase compositions of the obtained samples and crystal structures of the material at different state of charge (SoC) were characterized by means of powder X-ray diffraction (PXRD) using a Bruker D8 Advance diffractometer (Bragg-Brentano geometry, $CuK_{\alpha 1,2}$ radiation, LYNXEYE XE detector). JANA2006 and FullProf software were used for the pattern fitting and Rietveld refinement [20–22]. VESTA was used for the visualization of the crystal structures [23]. *Operando* PXRD patterns during the first galvanostatic charge-discharge were acquired at C/40 current density with the Bruker D8 Advance diffractometer using an electrochemical cell with a beryllium X-ray window. Investigation of the microstructure of the samples was performed with a field-emission scanning electron microscope (FE-SEM) Quattro S (FEI) and the chemical composition was determined using a dual beam scanning electron microscope Helios G4 PFIB UXe (FEI) equipped with an EDS system Octane Elite Super (EDAX).

The electrodes were prepared by grinding the material in a mortar and mixing first with carbon black Super P™ and then with polyvinylidene fluoride (PVDF) in the 70:20:10 mass ratio, respectively. The viscous electrode slurry was prepared by mixing the dry mixture with N-Methyl-2-pyrrolidone, 4 ml of the solvent being added to each gram of the dry mixture. The slurry was cast onto aluminum foil by tape-casting method, dried at 75 °C in air, cut into standard disk electrodes of 16 mm in diameter, which were then additionally dried under dynamic vacuum at 100 °C for 3 h. Two-electrode coin-type cells with potassium metal as the counter electrode were assembled in an MBraun glovebox under an Ar atmosphere using 0.6 mol/l solution of KPF_6 in a 1:1 mixture of ethylene carbonate and diethyl carbonate as electrolyte and borosilicate glass fiber membrane as a separator. Typical loading mass of the electrode active material was 8 mg. For the galvanostatic cycling the potentiostats/galvanostats Elins P20-X8 (ES8 software) and Bio-Logic SP-150 (EC-Lab software) were used.

All DFT calculations were performed in VASP program [24] using generalized gradient approximation (GGA) to exchange-correlation functional and standard PAW PBE pseudopotentials [25] with minimum number of valence electrons. Gaussian smearing with the width of 0.1 eV was used for Brillouin-zone integrations. The energy cut-off was fixed at 400 eV, the Gamma-centered k-point was 4x2x2 for the unit cell with 98 atoms. To eliminate Pulay errors the lattice optimization (ISIF = 4) was performed at constant volume for several contracted and expanded cells (7 points). The migration barriers were determined using nudged elastic band method as implemented in VASP using the unit cell. The method allows to find minimum energy path, which includes several intermediate configurations (images) between initial and final states. Five intermediate images were used. The optimization of atomic positions was performed using a quasi-Newton algorithm until the maximum force permitted for any vector component was less than 0.05 eV/ Å. The computational setup, including errors due to the periodic boundary conditions has been estimated to provide the precision of 0.1 eV for migration barriers.

3. Results and discussion

PXRD analysis of the phase composition (Fig. S1) identified the main phase as $K_6(VO)_2(V_2O_3)_2(PO_4)_4(P_2O_7)$ (PDF #01–075-4707) along with the impurities of $K_2VOP_2O_7$ (PDF #01–084-0011, 8.9(1) wt %, see the Rietveld refinement below) and β-$K_2(VO)_3(P_2O_7)_2$ (PDF #01–080-1208, 1.63(6) wt%, see the Rietveld refinement below). The SEM micrographs (Fig. 2a,b) demonstrate non-uniform size of the crystallites ranging between 0.1 and 5 μm. The EDX spectra (Fig. 2c) show the K:V:P atomic ratio of 1.00:1.01(6):1.04(8).

The crystal structure of $K_6(VO)_2(V_2O_3)_2(PO_4)_4(P_2O_7)$ is rather complex. Briefly, it can be described as consisting of infinite single chains of corner-sharing $V2O_6$ octahedra and double chains of $V1_2O_9$

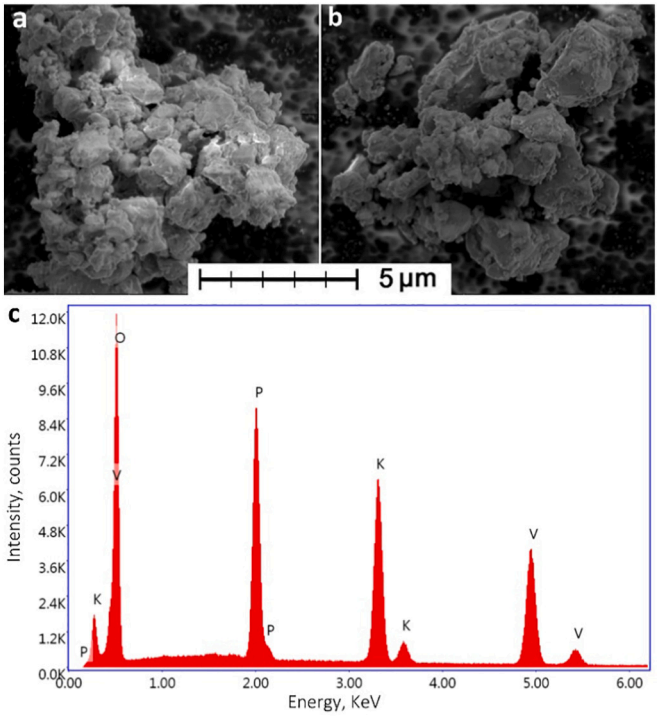

Fig. 2. The FE-SEM micrographs (a, b) and typical EDX spectrum (c) of $K_6(VO)_2(V_2O_3)_2(PO_4)_4(P_2O_7)$.

dimers of two corner-sharing $V1O_5$ tetragonal pyramids, and phosphate PO_4 and pyrophosphate P_2O_7 groups (Fig. 1). Both single and double chains run along the *a* axis being linked through the phosphate PO_4 tetrahedra into a three-dimensional framework. The framework contains spacious tunnels aligned along the *b* axis and populated with the K cations. The crystal structure can be described within an orthorhombic subcell with $a = 6.989$ Å, $b = 13.373$ Å, $c = 14.250$ Å and the *Pnma* space group [19]. With this unit cell and space symmetry the location of the pyrophosphate groups must be disordered: two possible energetically equivalent configurations of the P_2O_7 groups are transformed into each other by the *n*-glide plane and should stochastically occur in the structure in equal amounts. More detailed single crystal structural study revealed an orientational ordering of the P_2O_7 groups within a supercell of 4 times larger volume and triclinic symmetry [19]. This superstructure proposed in [Ref. 19] also features charge ordering of vanadium: one half of V^{4+} cations and all V^{5+} cations are placed in the $V2O_6$ octahedra and $V1O_5$ tetragonal pyramids, respectively; another half of V^{4+} cations also occupies $V1O_5$ pyramids along with V^{5+}, forming the superstructure. As the ordered structure model is prohibitively large for the Rietveld refinement from conventional PXRD data, the simpler disordered *Pnma* model was adopted for further structure refinements. Because of large number of variables, all atomic positions were refined with common atomic displacement parameter (ADP). The potassium occupancy factors in the pristine structure were refined revealing the values of 0.990(2) and 0.974(3) for the K1 and K2 positions, respectively, that is very close to the full occupancy, in agreement with the cationic composition measured by EDX. The $K_2VOP_2O_7$ and β-$K_2(VO)_3(P_2O_7)_2$ admixtures were also included into the refinement resulting in their mass fractions of 8.9(1) and 1.63(6) wt%, respectively. The experimental, calculated and difference PXRD profiles after the Rietveld refinement are shown in Fig. S1 of Supporting Information, main crystallographic parameters are provided in Table 1, the atomic coordinates are listed in Table S1 of Supporting Information. Similar refinement strategy was also applied to the crystal structures of the materials at different state of charge (Tables S2 - S4, Figs. S3 – S5).

The galvanostatic cycling of the first ten charge-discharge cycles with the rate of C/50 (1C = 88 mA/g) and the upper potential limit of 4.4 V vs. K/K^+ (except the first charge having the limit of 4.5 V) is demonstrated in Fig. 3a. It should be noted that as both $K_2VOP_2O_7$ and $K_2(VO)_3(P_2O_7)_2$ admixtures in the sample are electrochemically inert [16], the observed electrochemical activity is attributed solely to the $K_6(VO)_2(V_2O_3)_2(PO_4)_4(P_2O_7)$ phase. The first charge occurs through two sloping plateaus centered at ~4.1 and 4.4 V. Only the first plateau remains on discharge revealing a reversible capacity of 48 mAh/g. The high-voltage plateau is attributed to electrolyte decomposition and it was the reason for lowering the upper voltage limit from 4.5 to 4.4 V vs. K/K^+ in the subsequent cycles. The remarkable shifts of peaks on differential capacity curves evidence that there is growth of overall material resistance which can be attributed to the accumulation of the products of electrolyte oxidation on the surface of active particles (Fig. 3b). Cycling at a higher temperature of 60 °C and decreased voltage cutoff of 4.4 V vs. K/K^+ allow getting the same discharge capacity at a higher rate of C/20, as the one obtained at room temperature and slow rate of C/50, but unfortunately, the Coulombic efficiency drop is disproportionately high if the temperature is increased (Fig. S2).

Table 1
The main crystallographic parameters from the Rietveld refinements of $K_{6-x}(VO)_2(V_2O_3)_2(PO_4)_4(P_2O_7)$ in different states of charge.

		Pristine	Charged to 4.5 V	Discharged to 1.8 V
Space group			*Pnma*	
a, Å		6.9891(1)	7.1120(4)	6.9817(2)
b, Å		13.3735(2)	13.0850(5)	13.3826(5)
c, Å		14.2495(2)	14.1822(5)	14.2480(5)
V, Å^3		1331.89(6)	1319.8(1)	1331.3(1)
Occupancy	K1	0.990(2)	0.595(5)	0.989(3)
	K2	0.974(3)	0.551(5)	1.061(5)
Average V-O distance, Å	V1	2.002(4)	1.968(7)	2.034(5)
	V2	1.936(6)	1.909(10)	1.919(7)
Number of reflections		569	388	540
Number of parameters		38	37	37
R_P		0.063	0.011	0.017
wR_P		0.084	0.016	0.026
R_F		0.027	0.018	0.029
Goodness of fit		1.55	1.90	0.10

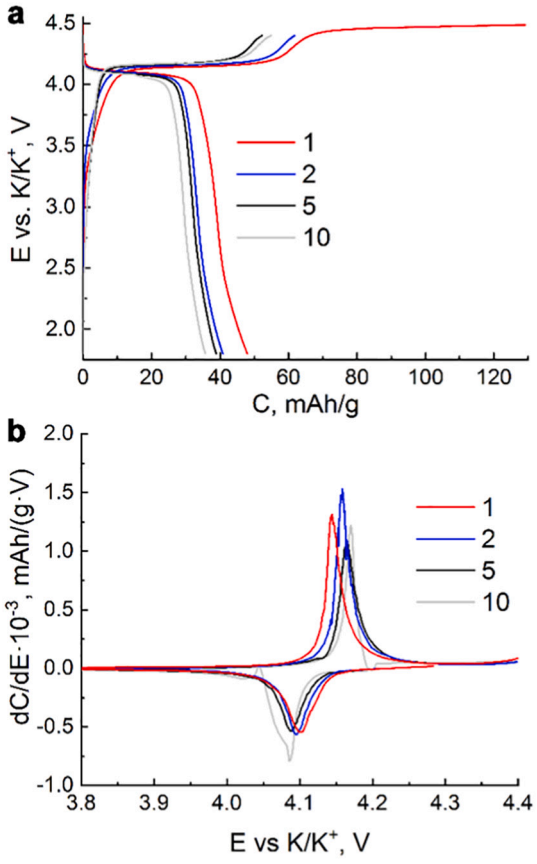

Fig. 3. (a) Galvanostatic charge-discharge (GSCD) curves of $K_6(VO)_2(V_2O_3)_2(PO_4)_4(P_2O_7)$ in a potassium-ion half-cell obtained at the current density C/50 at 25 °C (1st, 2nd, 5th and 10th cycles are plotted with the red, blue, black and grey colors respectively); (b) dC/dE plots obtained from the GSCD curves. (For interpretation of the references to colour in this figure legend, the reader is referred to the web version of this article.)

Ascribing the first plateau with the ~60 mAh/g charge capacity to the K-ion deinsertion from the $K_6(VO)_2(V_2O_3)_2(PO_4)_4(P_2O_7)$ structure is corroborated by the Rietveld-refined occupancy factors for the K1 and K2 positions in the material charged to 4.5 V (Table 1). They indicate the extraction of nearly 42% of potassium up to the $K_{3.5}(VO)_2(V_2O_3)_2(PO_4)_4(P_2O_7)$ composition (Table S2) that corresponds to 55 mAh/g capacity, in good agreement with the experimentally measured value. There is no drastic preference of the K1 and K2 positions for the K-ion deinsertion, although the K2 position delivers slightly more potassium than the K1 one. It should be noted that charging to 4.4 V allows extracting slightly less potassium (up to $K_{3.87}(VO)_2(V_2O_3)_2(PO_4)_4(P_2O_7)$ composition) corresponding to 47 mAh/g of reversible capacity (Table S3). Upon discharge, the K2 position restores its full occupancy, but about 1% of vacancies remain in the K1 position (Table S4). This corroborates the conjecture that > 4.5 V plateau is due to electrolyte decomposition. The average V-O distances shrink upon full charge for both V1 and V2 positions by 1.7% and 1.4%, respectively, indicating oxidation of the V cations. The

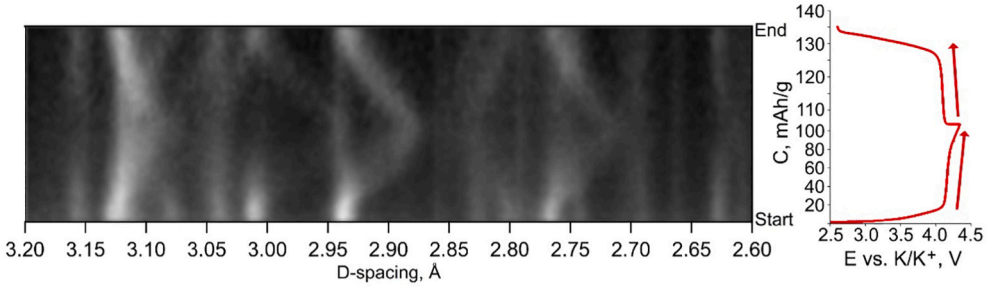

Fig. 4. *Operando* PXRD patterns during the first charge up to 4.4 V and a consequent discharge down to 2.6 V vs. K/K^+ with the current density of 2.2 mA/g (contour plot, left), and the corresponding cell voltage (right). The lower and upper halves of the picture correspond to the charge and discharge half-cycles. The background has been manually subtracted and the residual intensity has been normalized so that the maximum and minimum of intensity correspond to white and black colors, respectively.

concomitant volume change is, however, smaller and amounts to 0.9% only. Thus $K_6(VO)_2(V_2O_3)_2(PO_4)_4(P_2O_7)$ can virtually be considered as a "low strain" cathode, even in spite of relatively large size of deintercalated K^+ ions. Low Coulombic efficiency remaining for first 10 cycles could most probably be attributed to a reaction of cathode with the products of reduction of electrolyte with the potassium metal (so-called "chemical dialogue" [26]).

In order to get more insight into the charge-discharge mechanism, one galvanostatic cycle was conducted simultaneously with acquisition of *operando* PXRD patterns within the range of d-spacings between 3.2 and 2.6 Å (Fig. 4). The reflections demonstrate continuous displacement which is symmetrical upon charge and discharge that is an indicator of a solid-solution like behavior upon cycling.

The K^+ ion migration pathways and barriers were estimated with the DFT calculations. The simplified *Pnma* structure model (Fig. 1) used for the Rietveld refinement is inappropriate for DFT because it contains fractional occupancies due to stochastic arrangement of the pyrophosphate groups. However, ordered variants of the $K_6(VO)_2(V_2O_3)_2(PO_4)_4(P_2O_7)$ structure can be derived from the disordered *Pnma* model by appropriate symmetry reduction. The isotropy subgroups corresponding to the (0,0,0) k-vector (i.e. maintaining the same unit cell volume) have been found with the ISOTROPY software [27]. Two irreducible representations Γ_2^- and Γ_4^+ provide two ordered structures with $Pnm2_1$ and $P12_1/m1$ space groups, respectively. These hypothetical ordered structures were used for DFT analysis. It should be noted that the supercell published in [Ref. 19] consists of fragments which locally can be described by either $Pnm2_1$ or $P2_1/m$ space group and are arranged chequer-wise in the *ab* projection (Fig. 5a) overlapping by their halves.

To justify our approach, we compared atomic coordinates in the $Pnm2_1$ and $P2_1/m$ models with those in the supercell after atomic relaxation with DFT + U method. The obtained root mean square of atomic displacements between the models and supercell in both cases is less than 0.04 Å. Since on the course of K^+ ion migration the displacement of oxygen anions can exceed 0.4 Å, the small difference in atomic positions of 0.04 Å will have only negligible impact on the values of the K^+ migration barriers.

The optimized lattice constants for both $Pnm2_1$ and $P2_1/m$ unit cells were found to be very close to each other and equal to $a = 7.06$, $b = 13.63$ and $c = 14.56$ Å, respectively, which is about 2% larger than the experimental values in Table 1; such overestimation by GGA functional is a known issue for phosphate materials [28]. Both considered structures contain four non-equivalent K positions resulting in six unique shortest K-K migration hops (Fig. 5b, c).

The migration distances and barriers for both structures are collected in Table 2. We found that they have comparable migration barriers, the p4 barrier being lower in the $P2_1/m$ structure and p6 barrier being lower in the $Pnm2_1$ structure. The hops p1, p2, p4, and p6 have migration barriers of roughly 0.3–0.4 eV, while p3 and p5 hops have barriers of about 0.8 eV.

The continuous transport of K^+ involves combination of several hops. All possible combinations required for migration along the main crystallographic axes are provided in Table 3. Taking into account alternative migration routes and two variants of the structures, the resulting limiting barriers for K-ion transport along *a*, *b*, and *c* axes are 0.84, 0.31 and 0.84 eV, respectively. We conclude that the diffusivity has mainly one-dimensional nature, since barriers along *a* and *c* of 0.84 eV are notably higher than the empirically defined threshold of 0.5 eV required for satisfactory charge/discharge rate of an electrode material. At the same time, the obtained barrier of 0.31 eV for migration along *b* is comparable to that observed in $LiFePO_4$ [28], and only by 0.1 eV higher than the barrier in the recently discovered high-rate

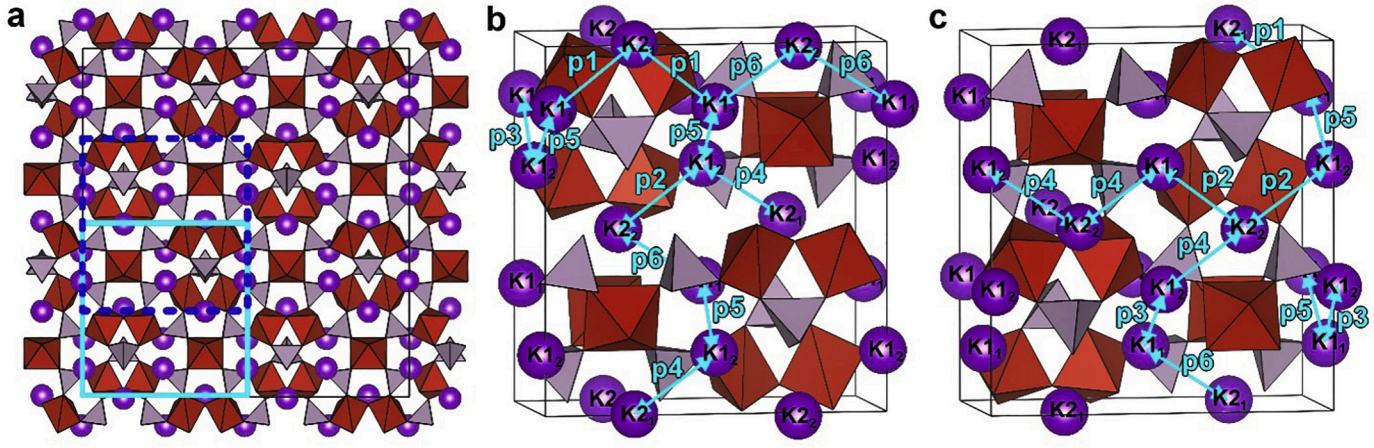

Fig. 5. (a) Projection *ab* of the supercell described in [Ref. 19] with distinguished fragments corresponding to the unit cells of the $Pnm2_1$ (dashed blue contour) and $P2_1/m$ (solid cyan contour) ordered models; (b, c) zoomed $Pnm2_1$ (b) and $P2_1/m$ (c) unit cells along with diffusion paths p*i* along the crystallographic axes *a*, *b* and *c* (see numerical data in Tables 2 and 3). Both models are represented in *bc* projection and additional potassium atoms are shown for better visibility of the diffusion paths. (For interpretation of the references to colour in this figure legend, the reader is referred to the web version of this article.)

Table 2
Length of migration hop, interatomic distance in the ideal crystal structure (Å) and the corresponding migration barriers calculated with NEB method (eV) for both crystal structures (*Pnm*2$_1$ and *P*2$_1$/*m*); n$_s$ is the number of K atom sitting at the end of the hop in the list of K atoms closest to the K sitting at the beginning of the hop.

Hop designation	Hop trajectory, n$_s$		d, Å		ΔE, eV	
	*Pnm*2$_1$	*P*2$_1$/*m*	*Pnm*2$_1$	*P*2$_1$/*m*	*Pnm*2$_1$	*P*2$_1$/*m*
p1	K1$_1$ – K2$_1$, 1	K1$_1$ – K2$_1$, 1	4.09	4.11	0.27	0.24
p2	K1$_2$ – K2$_2$, 1	K1$_2$ – K2$_2$, 1	4.21	4.19	0.32	0.31
p3	K1$_1$ – K1$_2$, 2	K1$_1$ – K1$_2$, 2	4.28	4.30	0.80	0.83
p4	K1$_2$ – K2$_1$, 3	K1$_2$ – K2$_2$, 3	4.38	4.34	0.38	0.28
p5	K1$_2$ – K1$_1$, 4	K1$_2$ – K1$_1$, 4	4.41	4.39	0.82	0.84
p6	K1$_1$ – K2$_2$, 4	K1$_1$ – K2$_1$, 4	4.47	4.51	0.27	0.42

Table 3
Pathways for continuous transport along main crystallographic axes and their effective migration barriers (eV) for the *Pnm*2$_1$ and *P*2$_1$/*m* structures and for the structure representing a mixture of both models.

Direction of diffusion	Combination of hops	ΔE$_p$, eV		
		*Pnm*2$_1$	*P*2$_1$/*m*	Mixture
Along *a*	p3 – p5	0.82	0.84	0.84
Along *b*	p6 – p1 – p1 – p6	0.27	0.42	0.31
	p4 – p2 – p2 – p4	0.38	0.31	
Along *c*	p1 – p5 – p2 – p6 – p5 – p4	0.82	–	0.84
	p1 – p5 – p4 – p1 – p5 – p4			
	p6 – p3 – p4 – p1 – p3 – p2	0.80		
	p6 – p3 – p2 – p6 – p3 – p2			
	p1 – p5 – p2 – p4 – p3 – p6	–	0.84	

$KVPO_4F$ cathode material [29]. Overall, the mobility of K^+ in $K_6(VO)_2(V_2O_3)_2(PO_4)_4(P_2O_7)$ should be fast, but because of essentially 1D character its practical realization requires dedicated shape of the crystallites with shortest dimension along the easiest diffusion direction *b*. Yet we considered two additional long migration hops along *a* and *c* axes, but the required barriers for migration in these cases are larger than 1.5 eV. However, under extraction of K^+ these barriers could be noticeably reduced. The dependence of migration barriers on K concentration requires further studies.

From Fig. 6a showing the topology of migration paths in the *Pnm*2$_1$ structure it is seen that the paths are almost straight with slight wriggling. The largest shuffling of the P and O atoms is observed for the p3 and p5 hops with the highest barriers of 0.8 eV. At saddle points the K^+ cations cross either a triangle (p1, p4, p6) or tetragon (p2, p3, p5) formed by oxygen anions, which approximately lie in one plane. The corresponding average K-O distances at the saddle point are 2.70, 2.73, 2.6, 2.58, 2.67, and 2.64 Å for the p1-p6 hops, respectively. It is hard to withdraw any relation between these distances and migration barriers. From the corresponding energy profiles compiled in Fig. 6b one can see that potassium has energy higher by roughly 0.1 eV in K1$_2$ and K2$_1$ positions than in K1$_1$ and K2$_2$ positions (notations from Fig. 5b). For all hops the saddle point is located near the middle of the path.

In order to understand the origin of higher migration barriers in the case of the p3 and p5 hops we used local descriptors [28], rationalizing the migration barriers in terms of site repulsive/attractive forces and lattice energies. The first descriptor is the change of average K-O distance between the saddle and minimum energy positions (Δd$_{av}$) on the course of K-ion migration. The calculated values of Δd$_{av}$ averaged by six nearest-neighbor oxygen atoms are provided in Table S5. It is seen that larger Δd$_{av}$ values correspond to larger DFT barriers. Since the average K-O distance is smaller at the saddle point we suggest that site repulsive energy has considerable contribution to the migration barrier. To check this conjecture, we calculated migration barriers using only site repulsive energies (ΔE$_{Born}$) obtained from the Gilbert parametrization with the parameters based on vibrational and crystallographic data [30]. The ΔE$_{Born}$ energies are provided in Table S5 showing good correlation with ΔE. Much larger repulsive energy barriers in case of the p3 and p5 hops highlight that the migration channels are simply too narrow for K-ion migration. Interestingly, in case of p1 and p6, the same DFT migration barriers correspond to different ΔE$_{Born}$ values. As we demonstrated in [Ref. 28] this can be related either to different site attractive or to lattice energy contributions.

4. Conclusions

$K_6(VO)_2(V_2O_3)_2(PO_4)_4(P_2O_7)$ was probed as a positive electrode for the K-ion batteries. It undergoes reversible electrochemical oxidation at the voltage of 4.1 ÷ 4.4 V vs. K/K^+ with extraction of more than 50% of potassium resulting in 47 mAh/g of reversible capacity with low volume change not exceeding 0.9%. Reversibility was shown by ex-situ XRPD of the discharged electrode and was confirmed by means of *operando* XRPD demonstrating a solid-solution mechanism of cycling for almost whole compositional range. Additionally, an investigation of the potassium diffusivity from the first principles has been conducted by

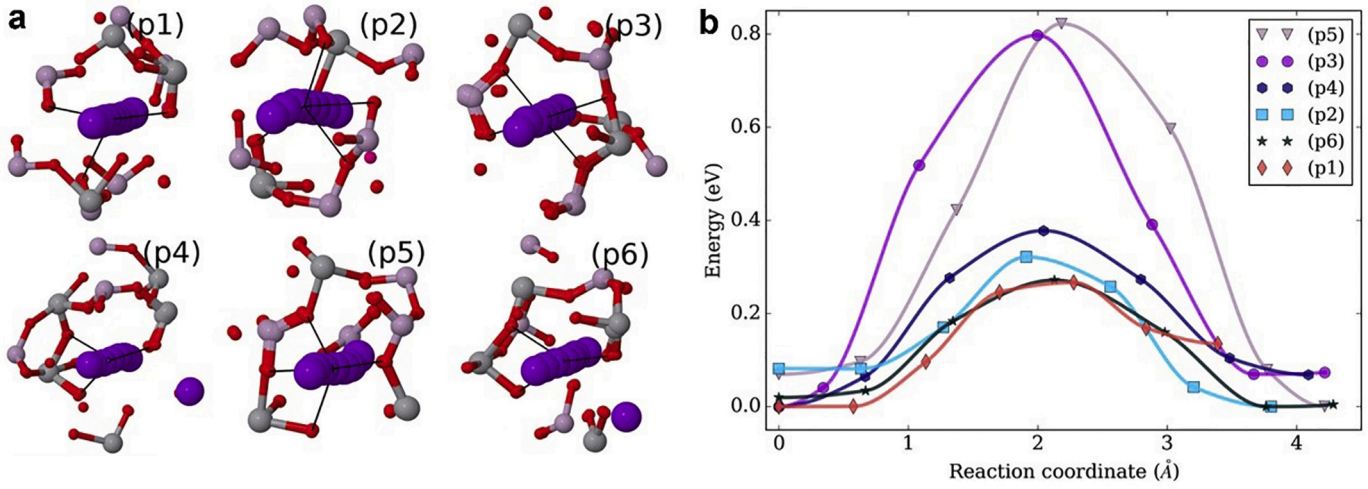

Fig. 6. (a) Overlapped atomic positions from every image obtained from optimization with NEB method in the *Pnm*2$_1$ structure (only representative nearest neighbor atoms from each image are shown). The black lines connect the middle atom of the hop reaction pathway with the nearest neighbor oxygen atoms forming a slightly distorted plane perpendicular to the local trajectory; (b) corresponding energy profiles for the investigated K-K migration hops.

the nudged elastic band method revealing the predominantly 1D character of K^+ diffusion along the *b*-axis with the energy barrier of 0.31 eV.

Declaration of Competing Interest

The authors declare that they have no known competing financial interests or personal relationships that could have appeared to influence the work reported in this paper.

Acknowledgement

Authors are grateful to the Russian Science Foundation (grant No. 17-73-30006) and to financial support from #2016-1/NGP.

Appendix A. Supplementary data

Supplementary data to this article can be found online at https://doi.org/10.1016/j.ssi.2020.115468.

References

[1] X. Jiang, et al., A Fe/Mn-based Prussian blue analogue as a K-rich cathode material for potassium-ion batteries, ChemElectroChem 4 (9) (2017) 2237–2242.
[2] L. Xue, et al., Low-cost high-energy potassium cathode, J. Am. Chem. Soc. 139 (6) (2017) 2164–2167.
[3] X. Bie, et al., A novel K-ion battery: hexacyanoferrate(ii)/graphite cell, J. Mater. Chem. A 5 (9) (2017) 4325–4330.
[4] G. He, L.F. Nazar, Crystallite size control of Prussian white analogues for nonaqueous potassium-ion batteries, ACS Energy Lett. 2 (5) (2017) 1122–1127.
[5] S.S. Fedotov, et al., AVPO4F (A = Li, K): A 4 v cathode material for high-power rechargeable batteries, Chem. Mater. 28 (2) (2016) 411–415.
[6] K. Chihara, et al., KVPO4F and KVOPO4 toward 4 volt-class potassium-ion batteries, Chem. Commun. 53 (37) (2017) 5208–5211.
[7] H. Kim, et al., A new strategy for high-voltage cathodes for K-Ion batteries: stoichiometric KVPO4F, Adv. Energy Mater. 8 (26) (2018) 1801591.
[8] X. Lin, et al., K3V2(PO4)2F3 as a robust cathode for potassium-ion batteries, Energy Storage Mater. 16 (2019) 97–101.
[9] N. Recham, et al., Preparation and characterization of a stable FeSO4F-based framework for alkali ion insertion electrodes, Chem. Mater. 24 (22) (2012) 4363–4370.
[10] C. Vaalma, et al., Non-aqueous K-Ion battery based on layered K0.3 MnO2 and hard carbon/carbon black, J. Electrochem. Soc. 163 (7) (2016) A1295–A1299.
[11] H. Kim, et al., Investigation of potassium storage in layered P3-type K0.5MnO2 cathode, Adv. Mater. 29 (37) (2017) 1702480.
[12] H. Kim, et al., K-Ion batteries based on a P2-type K0.6CoO2 cathode, Adv. Energy Mater. 7 (17) (2017) 1700098.
[13] Y. Hironaka, K. Kubota, S. Komaba, P2- and P3-KxCoO2 as an electrochemical potassium intercalation host, Chem. Commun. 53 (26) (2017) 3693–3696.
[14] T. Masese, et al., Rechargeable potassium-ion batteries with honeycomb-layered tellurates as high voltage cathodes and fast potassium-ion conductors, Nat. Commun. 9 (1) (2018) 3823.
[15] J. Han, et al., Investigation of K3V2(PO4)3/C nanocomposites as high-potential cathode materials for potassium-ion batteries, Chem. Commun. 53 (11) (2017) 1805–1808.
[16] W.B. Park, et al., KVP2O7 as a robust high-energy cathode for potassium-ion batteries: pinpointed by a full screening of the inorganic registry under specific search conditions, Adv. Energy Mater. 8 (13) (2018) 1703099.
[17] K. Kubota, et al., Towards K-Ion and Na-Ion Batteries as “Beyond Li-Ion”, Chem. Rec. 18 (4) (2018) 459–479.
[18] A. Gutierrez, N.A. Benedek, A. Manthiram Crystal-Chemical, Guide for understanding redox energy variations of M2+/3+ couples in polyanion cathodes for lithium-ion batteries, Chem. Mater. 25 (20) (2013) 4010–4016.
[19] A. Leclaire, B. Raveau, The actual structure of K6(VO)2(V2O3)2(PO4)4(P2O7): ordered distribution of P2O7 groups and charge ordering of vanadium, J. Solid State Chem. 179 (1) (2006) 205–211.
[20] V. Petříček, M. Dušek, L. Palatinus, Crystallographic computing system JANA2006: general features, Zeitschrift für Kristallogr. Crystall. Mater. 229 (2014) 345.
[21] J. Rodríguez-Carvajal, Recent advances in magnetic structure determination by neutron powder diffraction, Phys. B Condens. Matter 192 (1) (1993) 55–69.
[22] J. Rodriguez-Carvajal, T.J. Roisnel, FullProf.98 and WinPLOTR: new windows 95/NT applications for diffraction, Comm. Powder Diffr. Int. Union Crystallogr. 20 (May–August) (1998).
[23] K. Momma, F. Izumi, VESTA 3 for three-dimensional visualization of crystal, volumetric and morphology data, J. Appl. Crystallogr. 44 (6) (2011) 1272–1276.
[24] G. Kresse, J. Furthmüller, Efficiency of ab-initio total energy calculations for metals and semiconductors using a plane-wave basis set, Comput. Mater. Sci. 6 (1) (1996) 15–50.
[25] J.P. Perdew, K. Burke, M. Ernzerhof Generalized, Gradient approximation made simple, Phys. Rev. Lett. 77 (18) (1996) 3865–3868.
[26] L. Ellis, Probing the Causes and Effects of Parasitic Reactions in Lithium-Ion Cells, Dalhousie University, 2018.
[27] H.T. Stokes, et al., ISODISPLACE: a web-based tool for exploring structural distortions, J. Appl. Crystallogr. 39 (4) (2006) 607–614.
[28] D.A. Aksyonov, et al., Understanding migration barriers for monovalent ion insertion in transition metal oxide and phosphate based cathode materials: a DFT study, Comput. Mater. Sci. 154 (2018) 449–458.
[29] S.S. Fedotov, et al., Reversible facile Rb+ and K+ ions de/insertion in a KTiOPO4-type RbVPO4F cathode material, J. Mater. Chem. A 6 (29) (2018) 14420–14430.
[30] M. Kunz, T. Armbruster, Applications and limitations of the ionic potential model with empirically derived ion-specific repulsion parameters, Acta Crystallogr. Sect. B 48 (5) (1992) 609–622.